Solar and magnetic control of minor ion peaks in the dayside Martian ionosphere

J. -P. Huang[1], J. Cui[1,2,3], Y. -Q. Hao[4], J. -P. Guo[5], X. -S. Wu[2,3], D. -D. Niu[6], and Y. Wei[7]

[1]Planetary Environmental and Astrobiological Research Laboratory (PEARL), School of Atmospheric Sciences, Sun Yat-Sen University, Zhuhai, Guangdong, People's Republic of China
[2]National Astronomical Observatories, Chinese Academy of Sciences, Beijing, People's Republic of China
[3]Center for Excellence in Comparative Planetology, Chinese Academy of Sciences, Hefei, Anhui, People's Republic of China
[4]School of Earth and Space Sciences, Beijing University, Beijing, People's Republic of China
[5]Department of Astronomy, Beijing Normal University, Beijing, People's Republic of China
[6]Space Science Institute, Macau University of Science and Technology, Macau, People's Republic of China
[7]Institute of Geology and Geophysics, Chinese Academy of Sciences, Beijing, People's Republic of China

Key Points:

- The peak density and altitude for most minor ion species produced via direct photoionization show weak or no SZA variation.
- The minor ion peak density and altitude tend to increase significantly with increasing solar activity.
- The minor ion peak density and altitude show clear difference between the strongly and weakly magnetized regions.

Corresponding author: Jun Cui, cuijun7@mail.sysu.edu.cn

Abstract

The Neutral Gas and Ion Mass Spectrometer of the Mars Atmosphere and Volatile Evolution provides a large data set to explore the ion composition and structure of the Martian ionosphere. Here the dayside measurements are used to investigate the minor ion density profiles with distinctive peaks above 150 km, revealing a systematic trend of decreasing peak altitude with increasing ion mass. We specifically focus on a subset of species including O^+, N_2^+/CO^+, C^+, N^+, He^+, and O^{++}, all of which are mainly produced via direct photoionization of parent neutrals. Our analysis reveals weak or no variation with solar zenith angle (SZA) in both peak density and altitude, which is an expected result because these ion peaks are located within the optically thin regions subject to the same level of solar irradiance independent of SZA. In contrast, the solar cycle variations of peak density and altitude increase considerably with increasing solar activity, as a result of enhanced photoionization frequency and atmospheric expansion at high solar activities. He^+ serves as an exception in that its peak density increases towards large SZA and meanwhile shows no systematic variation with solar activity. The thermospheric He distribution on Mars should play an important role in determining these observed variations. Finally, the peak altitudes for all species are elevated by at least several km within the weakly magnetized regions, possibly attributable to the suppression of vertical diffusion by preferentially horizontal magnetic fields in these regions.

1 Introduction

Mars possesses a well-defined ionosphere on the sunlit side that is mainly produced by solar Extreme Ultraviolet (EUV) and X-ray ionization (Withers, 2009). The electron density distribution in the dayside Martian ionosphere has been extensively studied over the past few decades, thanks to a rich data set accumulated by both radio occultation and radar sounding experiments made on board several spacecrafts such as the Mars Global Surveyor (e.g. Tyler et al., 2001) and the Mars Express (e.g. Gurnett et al., 2005; Pätzold et al., 2005).

Existing analyses reveal that the electron density, N_e, near the main ionospheric peak varies with altitude, z, according to the Chapman theory formulated as

$$N_e = N_m \exp\left(\frac{1}{2}\left(1 - \frac{z - z_m}{H} - \exp\left(-\frac{z - z_m}{H}\right)\right)\right), \tag{1}$$

where N_m is the peak electron density, z_m is the peak electron altitude, and H is the scale height of the background neutral atmosphere (Chapman, 1931a, 1931b). This idealized theory predicts systematic variations of the peak electron density and altitude with both solar zenith angle (SZA) and solar EUV and X-ray flux, as fully supported by numerous studies available in the literature (e.g. Hantsch & Bauer, 1990; Morgan et al., 2008; Fox & Yeager, 2009; Fox & Weber, 2012; Yao et al., 2019). It is well-known that the peak electron altitude corresponds to where unit optical depth is reached due to atmospheric photoabsorption, implying that its location also responds to features in the background atmosphere such as the non-migrating tides (e.g. Bougher et al., 2001; Mendillo et al., 2017) and planet-encircling dust storms (e.g. Wang & Nielsen, 2003; Fang et al., 2020). Meanwhile, many studies have indicated clearly that the presence of strong crustal magnetic anomalies has an appreciable impact on the electron density distribution (e.g. Ness et al., 2000; Diéval et al., 2015; Venkateswara Rao et al., 2017; Diéval et al., 2018; Mohanamanasa et al., 2018; Fallows et al., 2019).

In contrast, the ion composition of the dayside Martian ionosphere was historically very limited, with only two individual measurements made by the Retarding Potential Analyzers (RPA) on board the Vikings 1 and 2, suggesting O_2^+ as the dominant ion species followed by O^+ and CO_2^+ (Hanson et al., 1977). Such a situation has been greatly improved with the arrival of the Mars Atmosphere and Volatile Evolution (MAVEN) space-

craft at the red planet in September 2014 (Jakosky et al., 2015), with its Neutral Gas and Ion Mass Spectrometer (NGIMS) capable of measuring a rich variety of species in the Martian ionosphere covering a broad mass range of 2-150 Da (Mahaffy et al., 2015). The preliminary NGIMS results revealed the presence of more than a dozen species persistently seen in the dayside Martian ionosphere (Benna, Mahaffy, Grebowsky, Fox, et al., 2015) and the presence of transient metallic ion species when Mars was perturbed by the near collision with Comet C/2013 A1 (Siding Spring) (Benna, Mahaffy, Grebowsky, Plane, et al., 2015).

With the aid of the large NGIMS data set, several recent studies have focused on the structural variability of various ion species in the dayside Martian ionosphere. During the nominal mission phase, the MAVEN periapsis was typically at 150-160 km, i.e., above the peak altitude of most ion species (e.g. Fox & Weber, 2012) and characterizing the topside ionosphere only. For instance, the NGIMS analysis of Wu et al. (2019) revealed a near constant density scale height of 100 km for all ion species on the dayside and meanwhile a clear impact of the ambient magnetic field configuration. A similar magnetic control of the ion distribution was obtained by Withers et al. (2019). Girazian, Halekas, et al. (2019) further reported that high Solar Wind (SW) dynamical pressures led to the depletion of all species in the topside Martian ionosphere, a trend persistently seen at all SZAs and in both strong and weak magnetic field regions.

Several ion species do show clear peak structures at high altitudes. For instance, the dayside O^+ peak was observed to be at 220-300 km and its variations with season, SZA, and solar ionizing flux were characterized by Girazian, Mahaffy, et al. (2019). Occasionally, the MAVEN spacecraft made Deep Dip (DD) campaigns down to a periapsis altitude as low as 120-130 km, allowing the properties near the main ionospheric peak, including the ion composition, to be investigated (Vogt et al., 2017). Despite the existing efforts, a variety of minor ion species in the dayside Martian ionosphere, with clear density peaks at sufficiently high altitudes to be sampled by the NGIMS during the nominal MAVEN mission phase, have not been explored in detail. This serves as the main motivation of the present study.

The paper is organized as follows. In Section 2, the peak densities and altitudes of minor ion species in the dayside median sense are derived, and the variability among different species is discussed. For a selected subset of minor ion species, the variations of their derived peak parameters, along with possible interpretations, are then presented. Specifically, we focus on the variations with SZA and solar activity in Section 3, as well as the variations with magnetic field configuration in Section 4. Finally, we discuss and draw conclusions in Section 5.

2 Parameterization of minor ion peaks

The analysis presented in this study relies mainly on the NGIMS ion density measurements made in the Open Source Ion mode, which are ideally suited for characterizing the structure and composition of the Martian ionosphere (Mahaffy et al., 2015). Here we include a total number of ~ 1100 dayside MAVEN orbits from October 2014 to June 2018, with periapsis SZA below 75° and irrespective of latitude, longitude, as well as solar activity. The dayside median density profiles of various ion species following the initial identification of Benna, Mahaffy, Grebowsky, Plane, et al. (2015) are displayed in Figure 1, from the typical MAVEN periapsis of 150 km during the nominal mission phase up to 450 km.

The figure reveals clearly the structural diversity of the Martian ionosphere with the detected ion species falling into two broad categories. On the one hand, the peak altitudes of a variety of ion species are located below the displayed altitude range, including the most dominant ion species, O_2^+, as well as some other ion species including CO_2^+,

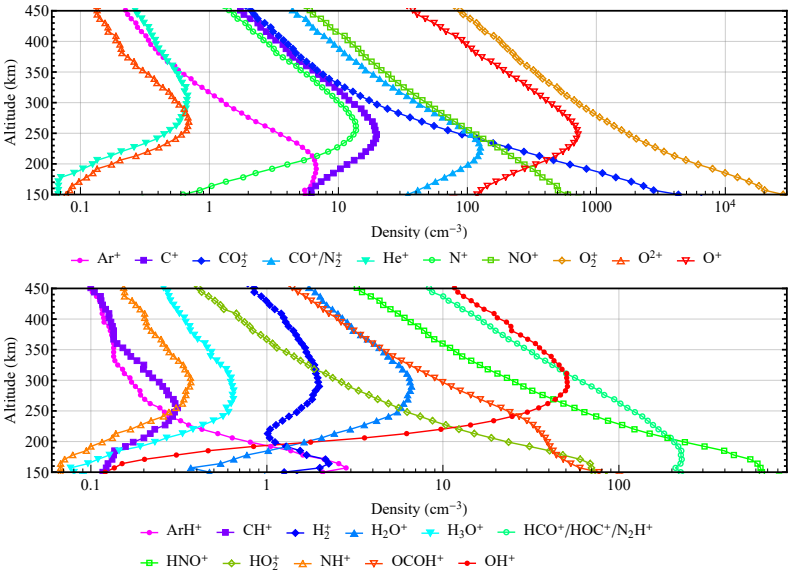

Figure 1. The structure of the dayside Martian ionosphere in terms of the median density profiles of all ion species measured by the NGIMS with SZA below 75° and reported in Benna, Mahaffy, Grebowsky, Plane, et al. (2015). While the peak altitude of the most abundant species, O_2^+, is clearly located below the lower boundary of 150 km, a variety of minor ion species present distinctive peaks at sufficiently high altitudes to be sampled by the NGIMS during the MAVEN nominal mission phase.

NO^+, and $OCOH^+$. On the other hand, many other minor ion species do present distinctive peaks above 150 km, including O^+, N_2^+/CO^+, C^+, N^+, Ar^+, O^{++}, He^+ in the top panel and $HCO^+/HOC^+/N_2H^+$, OH^+, H_2O^+, ArH^+, H_2^+, H_3O^+, NH^+, CH^+ in the bottom panel, both in the order of declining peak density. In addition, two species in the figure, HNO^+ and HO_2^+, marginally show the appearance of a layer structure peaked near 150 km. Note that CO^+ and N_2^+ cannot be distinguished by the NGIMS, with a mass resolution of 1 Da, due to their near equality in mass per charge (Mahaffy et al., 2015). HCO^+, HOC^+, and N_2H^+ cannot be distinguished for the same reason.

For the purpose of this study, we derive the peak parameters, including the peak density and peak altitude, from the observed distribution of each of the 15 minor ion species quoted above with clearly observed layer structures. This is implemented by an empirical fitting of the density profile within an altitude width of 60 km centered at the observed maximum using the idealized Chapman function given by Equation 1. The peak parameters are then straightforwardly given by the best-fit values of N_m and z_m in the equation for each species involved. We do not use directly the density and altitude of the observed maximum as the peak parameters in order to eliminate possible fluctuations in the ion density distribution forced either by gravity waves from below (e.g. England et al., 2017; Siddle et al., 2019) or by SW interactions from above (e.g. Kopf et al., 2008). While this may not be necessary for the situation depicted in Figure 1 since the ion density fluctuations have been effectively removed by combining all dayside measurements, we persist in applying the Chapman fitting throughout this study because we will encounter, in the following section, many cases for which the ion density profiles are not sufficiently smooth with localized irregularities superimposed on their large scale trends. A similar procedure has also been utilized to obtain the peak electron density and altitude from radio occultation measurements (e.g. Yao et al., 2019).

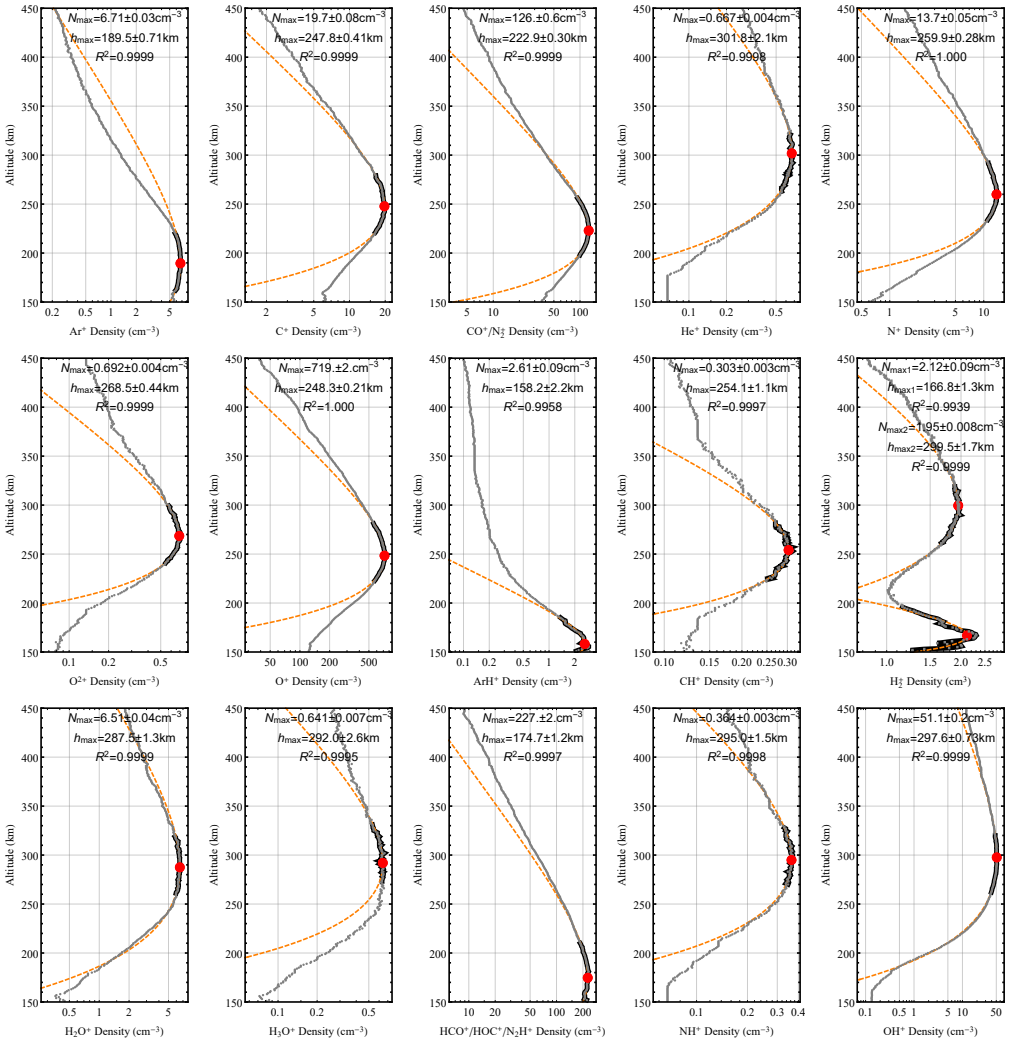

Figure 2. The dayside median density profiles of various ion species (grey dots), superimposed by the best-fit Chapman profiles (dashed orange lines). Each Chapman profile is constrained by the NGIMS measurements centered around the observed maximum with a common width of 60 km (black solid lines). The identified peaks are marked for clarification (red circles), with the best-fit peak parameters provided in the figure legend. Note that the dayside median H_2^+ distribution presents two peaks which are fitted separately.

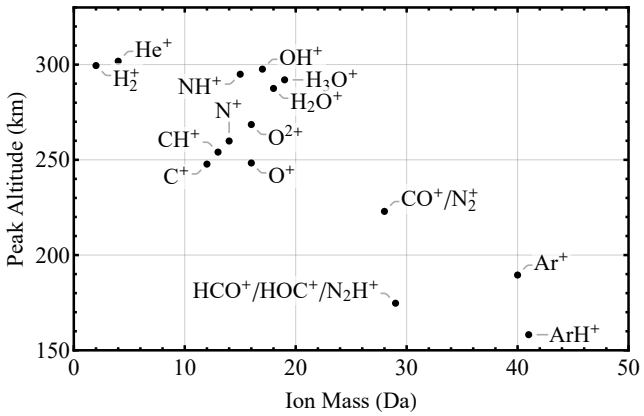

Figure 3. The derived minor ion peak altitude in the dayside median sense as a function of the ion mass, for all the 15 minor ion species displayed in Figures 1 and 2. The dayside median H_2^+ distribution presents two distinctive layer structures and only the peak altitude for the upper layer is indicated.

In Figure 2, we show the best-fit Chapman profiles superimposed on the dayside median NGIMS observations for all minor ion species with distinctive peak structures. In each panel, the portion of the NGIMS density profile used for constraining the peak parameters is indicated by the thick solid line, whereas the extension of the Chapman profile to the full displayed altitude range is indicated by the dashed line to demonstrate the restricted validity of the Chapman formulism in describing the minor ion distribution. The best-fit peak density and altitude appropriate for the dayside median situation, as well as their uncertainties, are provided in the figure legend of each panel for reference, along with the respective R^2 goodness-of-fit. Note that the H_2^+ distribution in the dayside Martian ionosphere is characterized by two separate peaks, including a lower one at 167 km and an upper one at 300 km, both with a peak density of around 2 cm^{-3}. The best-fit Chapman profiles for both peaks are indicated in Figure 2.

For the 15 species examined here, the peak density covers a wide range from 0.3 cm^{-3} for CH^+ to 720 cm^{-3} for O^+, which should rely on the abundances of their parent species in the ambient atmosphere and ionosphere as well as the efficiencies of their dominant chemical production and loss pathways involved (e.g. Krasnopolsky, 2002; Fox & Yeager, 2006; Fox, 2009; Matta et al., 2013; Fox, 2015). Of more interest is the observation of minor ion peak altitude that obviously decreases with increasing ion mass, as depicted in Figure 3. For H_2^+, only the peak altitude of the upper layer is indicated. According to the figure, the derived peak altitude ranges from around 300 km for relatively light ion species such as H_2^+ and He^+ to around 160 km for heavy ones such as ArH^+. Meanwhile, the observation that even heavier ion species such as CO_2^+ and $OCOH^+$ present layer structures below the altitude range displayed in Figures 1 and 2, along with the well established fact that the peak altitude of the dominant ion species, O_2^+, is at 130-140 km in the dayside median sense (e.g. Fox & Weber, 2012), is fully compatible with the aforementioned trend.

The observed mass dependence of ion peak altitude could be interpreted as follows. Unlike O_2^+ with peak altitude located within regions under near photochemical equilibrium (PCE), most of the species displayed in Figure 3 are peaked at high altitudes where the condition of PCE is violated (e.g. Mendillo et al., 2011). For such a situation, we may assume for simplicity that the ion peak altitude corresponds to where the ion diffusion and chemical loss timescales are identical. The ion diffusion timescale is proportional to the square of the ion scale height divided by the ion diffusion coefficient, of which

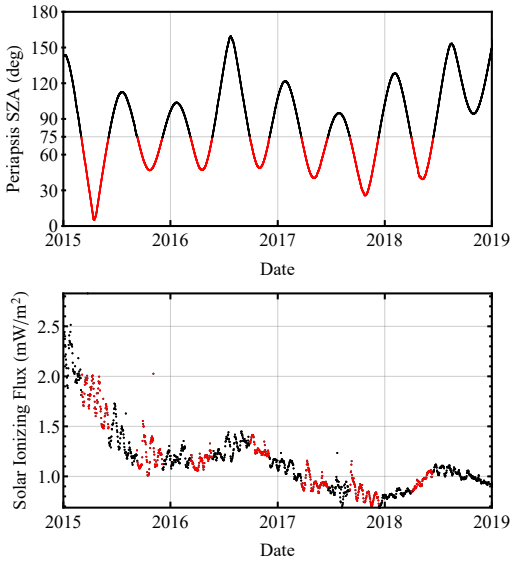

Figure 4. The distribution of the MAVEN orbits with respect to the periapsis SZA and solar ionizing flux, both as a function of the date of observation. The portion of the entire available data set included in this study is marked by red. The solar ionizing flux is obtained by integrating the solar EUV and X-ray model spectrum of Thiemann et al. (2017) over the wavelength range from 0.5 nm to 90 nm.

the former scales as M_i^{-2} and the latter scales as M_i^{-1} where M_i is the ion mass. Without loss of generality, we may further assume that for each ion species, the dominant chemical loss pathway is its reaction with CO_2, indicating that the CO_2 density right at the ion peak should be proportional to M_i. This naturally implies a higher ambient CO_2 density at the peak and consequently a lower peak altitude for heavy ion species as compared to light ones. The above line of reasoning is subject to several over-simplifications such as the neglect of the diversity of pathways for ion chemical loss and the neglect of the mass dependence of binary ion collision frequency. In addition, the peak altitudes of some species such as CO_2^+ and $OCOH^+$ are located within regions under PCE, implying a different mechanism responsible for the formation of their peaks from the mechanism addressed above. While a robust interpretation of the NGIMS observations shown in Figure 3 clearly relies on detailed photochemical model calculations, the simplified argument presented here is able to provide useful insights into the underlying physics and highlight the role of mass dependent ion diffusion in controlling the location of the ion density peak in the dayside Martian ionosphere.

3 Solar control of minor ion peak parameters

To investigate the variations of the minor ion peak structure with both SZA and solar activity, the Chapman fitting procedure outlined above is applied to the median ion density profiles obtained from a selected group of orbits in our sample, with the detailed scheme of grouping dependent on the variation that we intend to seek. The distribution of the MAVEN orbits used in this study is depicted in Figure 4 with respect to the periapsis SZA and solar ionizing flux, both as a function of the date of observation. The latter is obtained by integrating the solar EUV and X-ray model spectrum constructed with the aid of the MAVEN Extreme Ultraviolet Monitor band irradiance data (Eparvier et al., 2015; Thiemann et al., 2017). The integration is performed from 0.5 nm up to a maximum wavelength of 90 nm corresponding to the CO_2 ionization potential

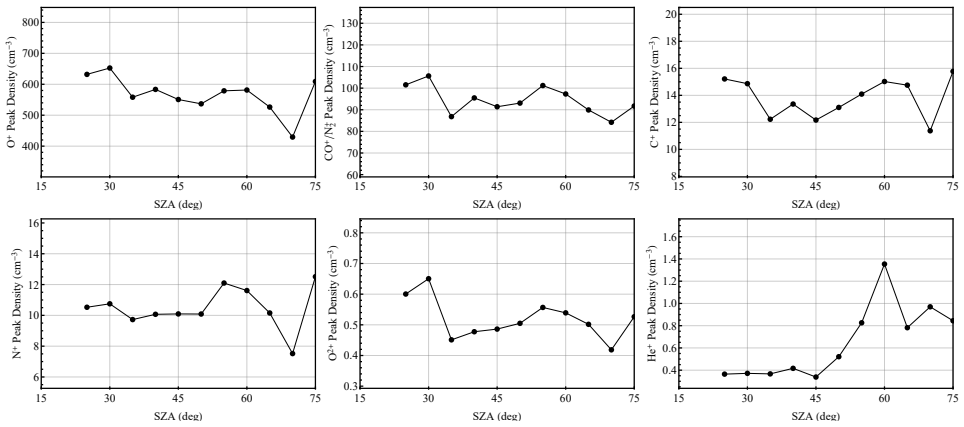

Figure 5. The SZA variations of the derived peak densities for various minor ion species in the dayside Martian ionosphere.

(Masuoka, 1994). The portion of the available data set included in this study is marked by red in the figure. Figure 4 demonstrates that the available NGIMS data set is not evenly sampled with low SZA measurements preferentially made at relatively high solar activities.

We consider in this study the SZA and solar cycle variations of a subset of minor ion species including O^+, N_2^+/CO^+, C^+, N^+, He^+, and O^{++}. A common feature of these species is that the dominant production channel is direct solar EUV and X-ray ionization. For instance, O^+ is mainly produced from both single photoionization of O and dissociative photoionization of CO or CO_2. Here Ar^+ is excluded as an exception because its peak is close to the lower boundary which, along with the broad appearance of the peak (see Figures 1 and 2), does not allow the peak parameters to be accurately determined in some cases. Several other species such as OH^+ and H_2O^+, though with clear peaks well characterized by the data, are not included in our investigation because they are mainly produced via ion-neutral reactions instead of direct photoionization. As an example, the reaction between O^+ and H_2, instead of the direct photoionization of H_2O, is the dominant channel producing ionospheric OH^+ on Mars due to the low H_2O abundance in the Martian upper atmosphere (e.g. Fox et al., 2015). As presented in Cui et al. (2020), the density variation of each of these species exhibits a very complicated pattern and possibly a strong dawn-dusk asymmetry.

We start with the SZA variations of the derived minor ion peak parameters. For this purpose, we divide the NGIMS data set into several subsamples, each covering a limited SZA range with a width of 5°. To avoid contamination by possible solar cycle variation (see below), we restrict our analysis to those measurements made with the solar ionizing flux in the range of 0.7-0.9 mW m^{-2}, appropriate for the low solar activity condition. The SZA variations of the derived peak parameters for all the 6 minor ion species are displayed in Figure 5 for peak density and Figure 6 for peak altitude, respectively. The uncertainties in these peak parameters, which are not displayed in the figures, are typically of comparably small amount as those quoted in Figure 2 legend due to the large number of orbits available for each subsample.

Despite the considerable scattering, both figures suggest weak or no SZA variation in either peak parameter over the SZA range from 25° to 75°. This is an expected result because the atmosphere should be optically thin near the peaks of the minor ion species involved here, implying that regions at different SZA feel roughly the same level of so-

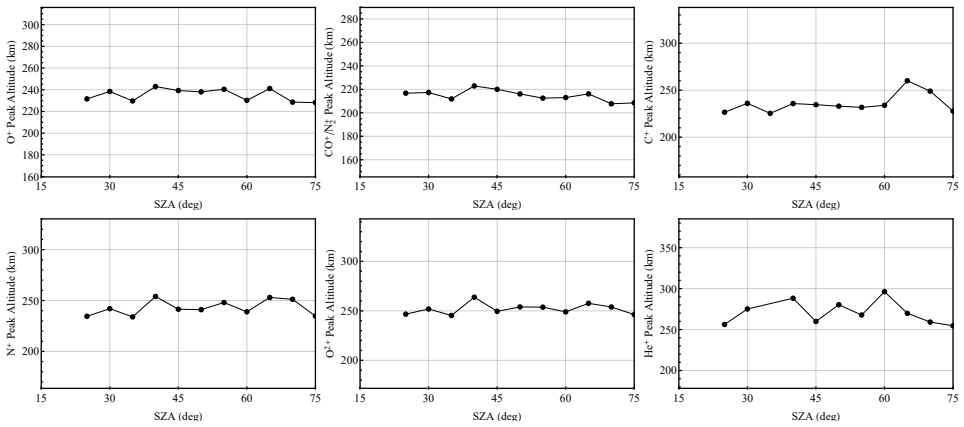

Figure 6. The SZA variations of the derived peak altitudes for various minor ion species in the dayside Martian ionosphere.

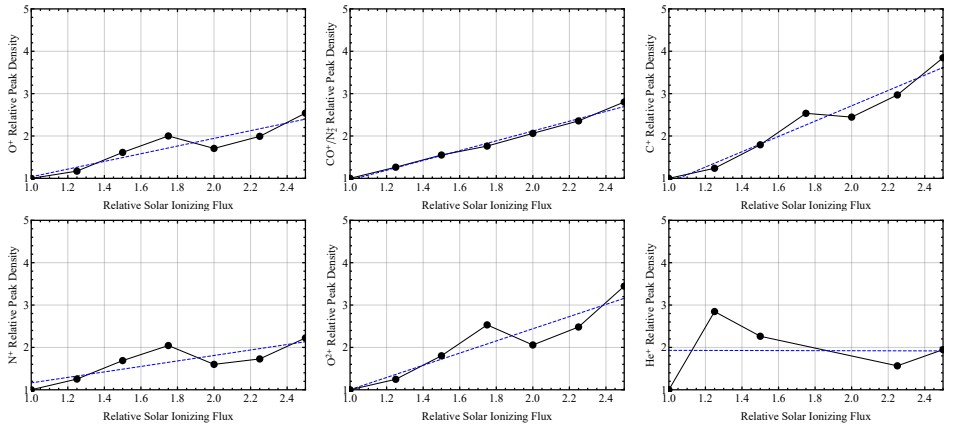

Figure 7. Similar to Figure 5 but for the minor ion peak density as a function of the solar ionizing flux (scaled by 0.8 mW m^{-2}). The dashed lines correspond to the best-fit power law relations given by Equation 2 in the text.

lar EUV and X-ray irradiance. The conclusion of either weak or no SZA variation for the O^+ peak parameters was also reported by Girazian, Mahaffy, et al. (2019).

In contrast, He^+ appears to be an exception with its peak density exhibiting a strong increasing trend towards the near terminator regions, despite that the peak altitude still remains roughly independent of SZA. Quantitatively, Figure 5 suggests that the peak density variation for the remaining 5 species is no more than 25% whereas the enhancement in the He^+ peak density at large SZA could reach more than a factor of 3 as compared to the low SZA value. This feature is indicative of an enhanced He abundance at large SZA in the ambient atmosphere caused by the subsidence in regions of horizontal wind convergence and the subsequent buildup of minor atmospheric species with large vertical scale heights such as H_2 and He (e.g. Elrod et al., 2017). The above discussions indicate that the SZA variation of a minor ion species in the dayside Martian ionosphere is strongly modulated by the variation of the background neutral atmosphere (e.g. Mendillo et al., 2017). Similar observations have also been reported for the diurnal variations of several protonated ion species (Cui et al., 2020).

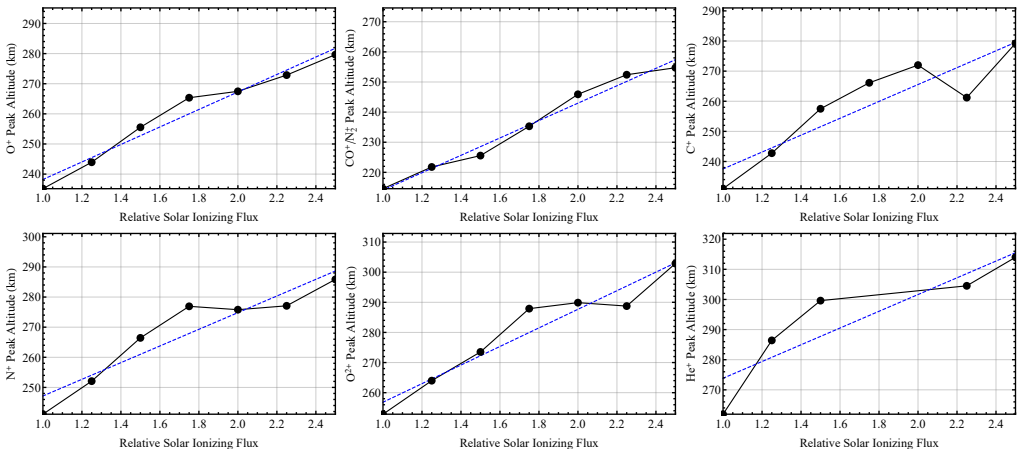

Figure 8. Similar to Figure 6 but for the minor ion peak altitude as a function of the solar ionizing flux (scaled by 0.8 mW m^{-2}). The dashed lines correspond to the best-fit linear relations given by Equation 3 in the text.

We next move on to the solar cycle variations of minor ion peak parameters by dividing the NGIMS data set into consecutive subsamples in increasing order of solar ionizing flux from 0.7 mW m^{-2} to 2.1 mW m^{-2} with a common interval of 0.2 mW m^{-2}. Due to the absence of any strong SZA variation in either peak parameter, we do not distinguish between different SZAs, except for He^+ which is restricted to the SZA range up to 50°. The variations of the derived peak parameters are shown in Figure 7 for peak density and Figure 8 for peak altitude, respectively. Our analysis reveals a systematic trend of increasing peak density and peak altitude with increasing solar ionizing flux for each species, again with He^+ being the only exception that does not reveal any unambiguous variation in its peak density. To be more quantitative, the corresponding Pearson correlation coefficients, denoted as R_i, are computed for all the 6 minor ion species and provided in Table 1 for reference.

The presence of strong solar cycle variation of the minor ion peak density is clearly linked to a higher photoionization frequency when subject to a more intense solar ionizing flux. A higher abundance of the parent neutrals likely makes a further contribution to the observed solar cycle variation, which is driven by enhanced photolysis of neutrals in the dayside Martian upper atmosphere. Meanwhile, the Martian atmosphere expands in response to increasing solar EUV and X-ray irradiance as indicated by a rising exobase altitude (Fu et al., 2020). This naturally moves the ionosphere to higher altitudes and causes the elevation of all minor ion peak altitudes, a mechanism that also accounts for the known effect of planet-encircling dust storms on the Martian ionospheric structure (e.g. Wang & Nielsen, 2003). The abnormal variation for He^+ peak density as displayed in Figure 7 is likely indicative of a lower He abundance in the dayside Martian upper atmosphere at higher solar activities, which counterbalances a higher He photoionization frequency. Without showing the details, we mention that our conjecture is verified by the NGIMS observation of a reduced He density from 7×10^4 cm^{-3} to 4×10^4 cm^{-3} when the solar ionizing flux increases from 0.8 mW m^{-2} to 2.0 mW m^{-2}, both referring to the respective He^+ peak altitude.

For a more quantitative parameterization of the observed solar cycle variations, they are described by a power law relation for peak density and a linear relation for peak altitude, in the forms of

$$N_{m,i} = \tilde{N}_{m,i} \left(\frac{I}{\tilde{I}} \right)^{\alpha_i}, \tag{2}$$

Table 1. The best-fit parameters for various minor ion species, including the linear Pearson correlation coefficients, R_i, the peak densities, $N_{m,i}$, the peak altitudes, $z_{m,i}$, as well as the power law indexes, α_i, and the linear slopes, β_i, that characterize the extent to which $N_{m,i}$ and $z_{m,i}$ vary with the solar ionizing flux (see Equations 2 and 3 in the text). Uncertainties for all parameters except for R_i are also provided. The parameters, $N_{m,i}$ and α_i, for He^+ peak density are not provided due to the absence of visible solar cycle variation.

Ion Species	Peak Altitude Parameters			Peak Density Parameters		
	R_i	$z_{m,i}$ (km)	β_i (km)	R_i	$N_{m,i}$ (cm^{-3})	α_i
O^+	0.982	209 ± 9	29 ± 5	0.948	562 ± 103	0.93 ± 0.28
N_2^+/CO^+	0.990	185 ± 7	29 ± 4	0.998	93 ± 4	1.09 ± 0.07
C^+	0.903	210 ± 22	28 ± 12	0.985	13 ± 2	1.45 ± 0.23
N^+	0.938	219 ± 17	28 ± 9	0.871	11 ± 3	0.73 ± 0.37
He^+	0.891	246 ± 34	28 ± 19	0.008	N/A	N/A
O^{++}	0.963	226 ± 14	31 ± 8	0.952	0.50 ± 0.12	1.25 ± 0.36

and

$$z_{m,i} = \tilde{z}_{m,i} + \beta_i \left(\frac{I}{\tilde{I}} \right), \tag{3}$$

where I is the solar ionizing flux defined in Section 2, $N_{m,i}$ and $z_{m,i}$ are the peak density and altitude for species i, $\tilde{N}_{m,i}$ and $\tilde{z}_{m,i}$ are the respective values for a reference ionizing flux of $\tilde{I} = 0.8$ mW m^{-2}, α_i and β_i are species dependent free parameters to be constrained by data-model comparison. The power law relation is implemented here to reflect the desired limiting behavior of zero peak density when the solar EUV and X-ray irradiance is switched off. The best-fit power law and linear models are superimposed in Figures 7 and 8 for comparison, with the respective best-fit parameters provided in Table 1.

Despite the considerable variability in minor ion peak altitude suggested by the NGIMS measurements (see Section 2), different species are characterized by a comparable increase in peak altitude, which is on average 44 km over the solar ionizing flux range displayed in Figure 8. In contrast, the extent to which the peak density varies with solar activity differs substantially from species to species. Neglecting He^+, the variation is maximized for C^+ with a power index of ~ 1.5 and minimized for N^+ with a power index of ~ 0.7. The derived power indexes suggest that over the available range of solar ionizing flux, the C^+ peak density increases by a factor of nearly 4 and the N^+ peak density increases by a factor of 2 only. It is interesting to note from Table 1 that both the O^+ and N_2^+/CO^+ peak densities are almost linearly correlated with the solar ionizing flux.

4 Magnetic control of minor ion peak parameters

In this section, we further investigate for O^+, N_2^+/CO^+, C^+, N^+, He^+, and O^{++} the variations of their peak parameters with the ambient magnetic field configuration, characterized by both draped fields formed via SW interactions (e.g. Brain et al., 2006) and crustal fields that tend to distribute over the southern hemisphere of Mars (e.g. Langlais et al., 2019). Again to avoid contamination by the strong solar cycle variation, our analysis is restricted to NGIMS measurements made with the solar ionizing flux in the range of 0.7-0.9 mW m^{-2} appropriate for the low solar activity condition. For our purpose, two subsamples are defined, one for weak magnetic field regions with crustal field intensity below 10 nT and the other one for strong magnetic field regions with crustal field intensity above 30 nT, where the crustal magnetic field model at a fixed altitude of 400 km

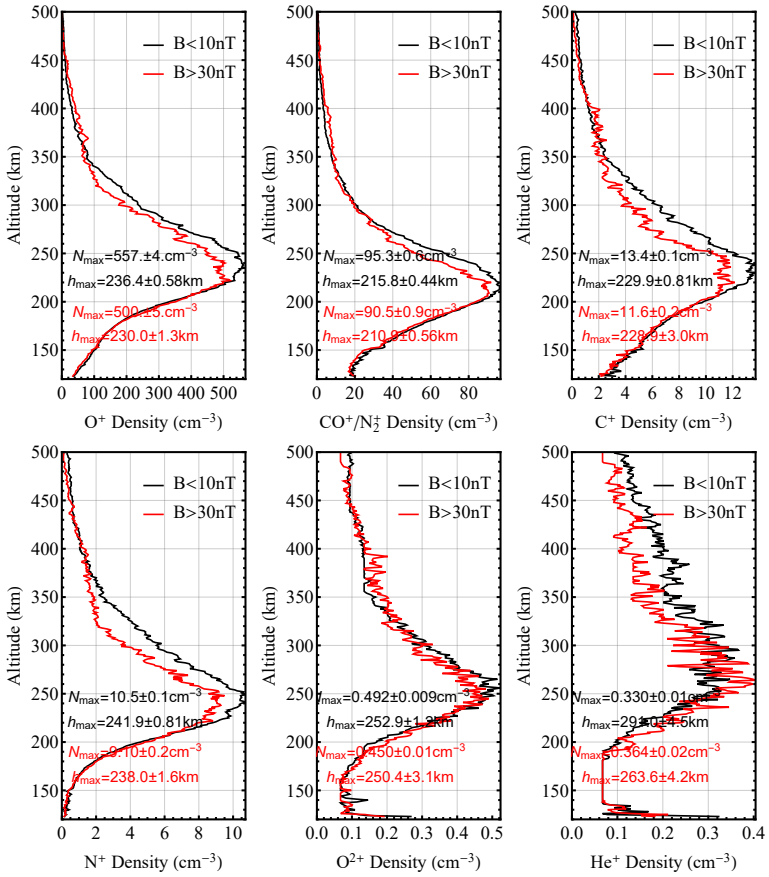

Figure 9. A comparison of the minor ion density profiles between strongly and weakly magnetized regions, defined with the crustal field intensity below 10 nT and above 30 nT, respectively, at a reference altitude of 400 km according to the model of Langlais et al. (2019).

based on Langlais et al. (2019) is used. The minor ion density profiles for the two subsamples are compared in Figure 9, where both ion peaks are indicated by the solid circles. The best-fit Chapman profiles are not shown in the figure to avoid over-crowdedness, but the best-fit peak parameters are indicated in the figure legend for reference.

The figure shows clearly that the density profiles for both regions are similar below 200 km, whereas at higher altitudes, the minor ion densities, including the peak densities, within the strongly magnetized regions tend to be considerably reduced up to at least 350 km as compared to the weakly magnetized regions. Meanwhile, the magnetic control of minor ion peak altitude is also visible in Figure 9 in that the peak altitude tends to be higher when the ambient magnetic fields are weaker. To be more quantitative, the variation of peak density with magnetic field intensity is maximized for C^+ and N^+ with an enhancement of more than 15% near weak magnetic fields, whereas the variation of peak altitude is maximized for He^+ with an elevation by 27 km in the same regions. A similar magnetic control of O^+ density above 200 km has recently been reported by Withers et al. (2019).

The effect of ambient magnetic fields on the Martian ionosphere occurs mainly via modification of plasma diffusion (e.g. Shinagawa & Cravens, 1989; Matta et al., 2015). Below 200 km, the effect of diffusion is usually negligible (e.g. Mendillo et al., 2011; Mukundan et al., 2020), which is responsible for the absence of magnetic control at these al-

titudes in Figure 9. At higher altitudes, the effect of diffusion is critically dependent on the ambient magnetic field configuration. Recent investigations (e.g. Xu et al., 2017) indicate that the magnetic field lines tend to be more horizontal in the weakly magnetized regions, implying a reduced effect of vertical diffusion relative to the strongly magnetized regions with preferentially vertical field lines (see also Wu et al., 2019). This naturally leads to an elevated minor ion peak altitude as observed. Meanwhile, when subject to the same level of solar EUV and X-ray irradiance, the total content of ions is unchanged but they are redistributed by vertical diffusion which is responsible for a reduced density profile from 200 km to at least 350 km incorporating the peak region. The observation reported here has to be distinguished from that of Wu et al. (2019) focusing on the dayside regions well above the minor ion peaks and suggesting instead an enhanced distribution near strong magnetic fields. The combination of the two works provides a more thorough picture of the structural variability of minor ion distribution over the full altitude range sampled by the NGIMS during the MAVEN nominal mission phase.

5 Discussions and Conclusions

Historically, the ion composition of the Martian ionosphere was only available from the RPA measurements made on board the Vikings 1 and 2 (Hanson et al., 1977). The extensive data set accumulated by the MAVEN NGIMS has provided a unique opportunity to explore the structural variability of the Martian ionosphere in terms of the minor ion distribution (Mahaffy et al., 2015). The dayside median density profiles of many ion species detected by the NGIMS show distinctive layers peaked above 150 km, the typical periapsis altitude during the nominal mission phase (Benna, Mahaffy, Grebowsky, Fox, et al., 2015). Whenever possible, the peak parameters for each ion species, including the peak density and peak altitude, are derived from the idealized Chapman fitting to the measured densities over a restricted altitude range centered at the observed maximum.

The derived peak altitude shows a clear anti-correlation with the ion mass, from around 160 km for heavy species such as ArH^+ to more than 300 km for light species such as He^+ and H_2^+. Assuming that the minor ion peak altitude is controlled by where the ion chemical loss and diffusion timescales become equal, we propose a simplified argument to interpret the above observation, predicting that the ambient atmospheric density at the ion peak should be roughly proportional to the ion mass. This naturally accounts for an elevated peak altitude for relatively light ion species as revealed by the NGIMS measurements.

We further investigate the solar control of a selected subset of minor ion species with (1) distinctive peak structures above 150 km and (2) chemical production pathways dominated by the direct photoionization of their parent neutrals. These ions include O^+, N_2^+/CO^+, C^+, N^+, He^+, and O^{++} in the order of decreasing dayside median peak density. For most species, both their peak densities and altitudes show either weak or no variation with SZA, which is an expected result because the atmosphere is optically thin near the peaks, implying that regions at different SZA feel roughly the same level of solar EUV and X-ray irradiance. The conclusion of weak or no SZA variation for the ion peak parameters was also reported by Girazian, Mahaffy, et al. (2019), but for O^+ only. For He^+ as an exception, a substantial increase in peak density towards large SZA is suggested by the data, despite that the peak altitude still remains roughly constant. The strong SZA variation in He^+ peak density, which is compatible with the diurnal variations of several protonated species as recently reported by Cui et al. (2020), could be interpreted as driven by the variation of He in the ambient atmosphere, as a result of the subsidence in regions of horizontal wind convergence and the subsequent buildup of minor atmospheric species with large vertical scale heights including He (Elrod et al., 2017).

The solar cycle variations of minor ion peak density and altitude are characterized by a clear increase in either parameter with increasing solar ionizing flux, which is persistently seen for all species investigated here except for He^+. The variation in peak density is clearly the result of an enhanced photoionization frequency at high solar activities, whereas the variation in peak altitude is caused by the expansion of the Martian upper atmosphere and the consequent elevation of the ionospheric layer structure also at high solar activities. It is interesting to note that the increase in peak altitude with increasing solar ionizing flux is of comparable amount for all species, by 44 km over the solar ionizing flux range from 0.8 mW m^{-2} to 2.0 mW m^{-2}, but the increase in peak density differs substantially among various minor ion species. For He^+ as an exception, no clear solar cycle variation in peak density is observed despite that the peak altitude still increases with increasing solar activity as normal. This is likely indicative of a reduction in thermospheric He abundance at high solar activities which counterbalances a simultaneous enhancement in He photoionization frequency.

Finally, the difference in minor ion peak parameters between strongly and weakly magnetized regions is examined. Despite that no magnetic control of minor ion distribution is found below 200 km, the difference in ion distribution between different magnetic field intensities is distinctive above 200 km, manifest as an enhanced ion distribution up to at least 350 km in weakly magnetized regions. A similar magnetic control was recently reported by Withers et al. (2019) for the three most abundant species, O_2^+, O^+, and CO_2^+, in the Martian ionosphere. In addition, the minor ion peak altitude tends to be elevated by at least several km in weakly magnetized regions. We propose that such an observation is related to the preference of more horizontal field lines in weakly magnetized regions (e.g. Xu et al., 2017; Wu et al., 2019), which suppresses the effect of vertical ion diffusion relative to local chemical loss and thus moves the ion peak to a higher altitude.

The results presented here are useful towards establishing an overall picture of the structural variability of minor ion distribution in the dayside Martian ionosphere, highlighting the roles of solar illumination and magnetic field configuration as controlling factors. These results are well suited for follow-up comparisons with realistic photochemical model calculations (e.g. Shinagawa & Cravens, 1989; Krasnopolsky, 2002; Fox & Yeager, 2006; Fox, 2009; Matta et al., 2013; Fox, 2015; Matta et al., 2015). However, we caution that the present study relies on the analysis of a small portion of minor ion species detected by the NGIMS. A thorough investigation of additional species, of which the chemical production channels are diverse and not restricted to direct photoionization of parent neutrals, may demonstrate a more complicated pattern of spatial and temporal variations.

Acknowledgments

This work is supported by the B-type Strategic Priority Program No. XDB41000000 funded by the Chinese Academy of Sciences and the pre-research project on Civil Aerospace Technologies No. D020105 funded by China's National Space Administration. The authors also acknowledge supports from the National Science Foundation of China through grants 41525015, 41525016, 41774186, and 41904154. The MAVEN data set used in this work is publicly available at the MAVEN Science Data Center (http://lasp.colorado.edu/maven/sdc/public/).

References

Benna, M., Mahaffy, P. R., Grebowsky, J. M., Fox, J. L., Yelle, R. V., & Jakosky, B. M. (2015, November). First measurements of composition and dynamics of the Martian ionosphere by MAVEN's Neutral Gas and Ion Mass Spectrometer. *Geophysical Research Letters*, *42*(21), 8958-8965. doi: 10.1002/2015GL066146

Benna, M., Mahaffy, P. R., Grebowsky, J. M., Plane, J. M. C., Yelle, R. V., & Jakosky, B. M. (2015, June). Metallic ions in the upper atmosphere of Mars from the passage of comet C/2013 A1 (Siding Spring). *Geophysical Research Letters*, *42*(12), 4670-4675. doi: 10.1002/2015GL064159

Bougher, S. W., Engel, S., Hinson, D. P., & Forbes, J. M. (2001, January). Mars Global Surveyor radio science electron density profiles : Neutral atmosphere implications. *Geophysical Research Letters*, *28*(16), 3091-3094. doi: 10.1029/2001GL012884

Brain, D. A., Mitchell, D. L., & Halekas, J. S. (2006, June). The magnetic field draping direction at Mars from April 1999 through August 2004. *Icarus*, *182*(2), 464-473. doi: 10.1016/j.icarus.2005.09.023

Chapman, S. (1931a, January). The absorption and dissociative or ionizing effect of monochromatic radiation in an atmosphere on a rotating earth. *Proceedings of the Physical Society*, *43*(1), 26-45. doi: 10.1088/0959-5309/43/1/305

Chapman, S. (1931b, September). The absorption and dissociative or ionizing effect of monochromatic radiation in an atmosphere on a rotating earth part II. Grazing incidence. *Proceedings of the Physical Society*, *43*(5), 483-501. doi: 10.1088/0959-5309/43/5/302

Cui, J., Ren, Z., Wu, Z., Wu, X., Hao, Y., & Wei, Y. (2020, May). Abnormal dawn-dusk asymmetry of protonated ions in the Martian ionosphere. *The Astrophysical Journal Letters*, *XXX*(X), XXXX-XXXX. doi: XXXXXXXXXX

Diéval, C., Andrews, D. J., Morgan, D. D., Brain, D. A., & Gurnett, D. A. (2015, September). MARSIS remote sounding of localized density structures in the dayside Martian ionosphere: A study of controlling parameters. *Journal of Geophysical Research (Space Physics)*, *120*(9), 8125-8145. doi: 10.1002/2015JA021486

Diéval, C., Kopf, A. J., & Wild, J. A. (2018, May). Shapes of Magnetically Controlled Electron Density Structures in the Dayside Martian Ionosphere. *Journal of Geophysical Research (Space Physics)*, *123*(5), 3919-3942. doi: 10.1002/2017JA025140

Elrod, M. K., Bougher, S., Bell, J., Mahaffy, P. R., Benna, M., Stone, S., ... Jakosky, B. (2017, February). He bulge revealed: He and CO_2 diurnal and seasonal variations in the upper atmosphere of Mars as detected by MAVEN NGIMS. *Journal of Geophysical Research (Space Physics)*, *122*(2), 2564-2573. doi: 10.1002/2016JA023482

England, S. L., Liu, G., Yiğit, E., Mahaffy, P. R., Elrod, M., Benna, M., ... Jakosky, B. (2017, February). MAVEN NGIMS observations of atmospheric gravity waves in the Martian thermosphere. *Journal of Geophysical Research (Space Physics)*, *122*(2), 2310-2335. doi: 10.1002/2016JA023475

Eparvier, F. G., Chamberlin, P. C., Woods, T. N., & Thiemann, E. M. B. (2015, December). The Solar Extreme Ultraviolet Monitor for MAVEN. *Space Science Reviews*, *195*(1-4), 293-301. doi: 10.1007/s11214-015-0195-2

Fallows, K., Withers, P., Morgan, D., & Kopf, A. (2019, July). Extremely High Plasma Densities in the Mars Ionosphere Associated With Cusp-Like Magnetic Fields. *Journal of Geophysical Research (Space Physics)*, *124*(7), 6029-6046. doi: 10.1029/2019JA026690

Fang, X., Ma, Y., Lee, Y., Bougher, S., Liu, G., Benna, M., ... Jakosky, B. (2020, March). Mars Dust Storm Effects in the Ionosphere and Magnetosphere and Implications for Atmospheric Carbon Loss. *Journal of Geophysical Research (Space Physics)*, *125*(3), e26838. doi: 10.1029/2019JA026838

Fox, J. L. (2009, December). Morphology of the dayside ionosphere of Mars: Implications for ion outflows. *Journal of Geophysical Research (Planets)*, *114*(E12), E12005. doi: 10.1029/2009JE003432

Fox, J. L. (2015, May). The chemistry of protonated species in the martian ionosphere. *Icarus*, *252*, 366-392. doi: 10.1016/j.icarus.2015.01.010

Fox, J. L., Benna, M., Mahaffy, P. R., & Jakosky, B. M. (2015, November). Water and water ions in the Martian thermosphere/ionosphere. *Geophysical Research Letters*, *42*(21), 8977-8985. doi: 10.1002/2015GL065465

Fox, J. L., & Weber, A. J. (2012, November). MGS electron density profiles: Analysis and modeling of peak altitudes. *Icarus*, *221*(2), 1002-1019. doi: 10.1016/j.icarus.2012.10.002

Fox, J. L., & Yeager, K. E. (2006, October). Morphology of the near-terminator Martian ionosphere: A comparison of models and data. *Journal of Geophysical Research (Space Physics)*, *111*(A10), A10309. doi: 10.1029/2006JA011697

Fox, J. L., & Yeager, K. E. (2009, April). MGS electron density profiles: Analysis of the peak magnitudes. *Icarus*, *200*(2), 468-479. doi: 10.1016/j.icarus.2008.12.002

Fu, M., Cui, J., Wu, X., Wu, Z., & Li, J. (2020, February). The variations of the Martian exobase altitude. *Earth and Planetary Physics*, *4*(1), 4-10. doi: 10.26464/epp2020010

Girazian, Z., Halekas, J., Morgan, D. D., Kopf, A. J., Gurnett, D. A., & Chu, F. (2019, August). The Effects of Solar Wind Dynamic Pressure on the Structure of the Topside Ionosphere of Mars. *Geophysical Research Letters*, *46*(15), 8652-8662. doi: 10.1029/2019GL083643

Girazian, Z., Mahaffy, P., Lee, Y., & Thiemann, E. M. B. (2019, April). Seasonal, Solar Zenith Angle, and Solar Flux Variations of O^+ in the Topside Ionosphere of Mars. *Journal of Geophysical Research (Space Physics)*, *124*(4), 3125-3138. doi: 10.1029/2018JA026086

Gurnett, D. A., Kirchner, D. L., Huff, R. L., Morgan, D. D., Persoon, A. M., Averkamp, T. F., ... Picardi, G. (2005, December). Radar Soundings of the Ionosphere of Mars. *Science*, *310*(5756), 1929-1933. doi: 10.1126/science.1121868

Hanson, W. B., Sanatani, S., & Zuccaro, D. R. (1977, September). The Martian ionosphere as observed by the Viking retarding potential analyzers. *Journal of Geophysical Research*, *82*(B28), 4351-4363. doi: 10.1029/JS082i028p04351

Hantsch, M. H., & Bauer, S. J. (1990, April). Solar control of the Mars ionosphere. *Planetary and Space Science*, *38*(4), 539-542. doi: 10.1016/0032-0633(90)90146-H

Jakosky, B. M., Grebowsky, J. M., Luhmann, J. G., & Brain, D. A. (2015, November). Initial results from the MAVEN mission to Mars. *Geophysical Research Letters*, *42*(21), 8791-8802. doi: 10.1002/2015GL065271

Kopf, A. J., Gurnett, D. A., Morgan, D. D., & Kirchner, D. L. (2008, September). Transient layers in the topside ionosphere of Mars. *Geophysical Research Letters*, *35*(17), L17102. doi: 10.1029/2008GL034948

Krasnopolsky, V. A. (2002, December). Mars' upper atmosphere and ionosphere at low, medium, and high solar activities: Implications for evolution of water. *Journal of Geophysical Research (Planets)*, *107*(E12), 5128. doi: 10.1029/2001JE001809

Langlais, B., Thébault, E., Houliez, A., Purucker, M. E., & Lillis, R. J. (2019, June). A New Model of the Crustal Magnetic Field of Mars Using MGS and MAVEN. *Journal of Geophysical Research (Planets)*, *124*(6), 1542-1569. doi: 10.1029/2018JE005854

Mahaffy, P. R., Benna, M., King, T., Harpold, D. N., Arvey, R., Barciniak, M., ... Nolan, J. T. (2015, December). The Neutral Gas and Ion Mass Spectrometer on the Mars Atmosphere and Volatile Evolution Mission. *Space Science Reviews*, *195*(1-4), 49-73. doi: 10.1007/s11214-014-0091-1

Masuoka, T. (1994, November). Single- and double-photoionization cross sections of carbon dioxide (CO_2) and ionic fragmentation of $CO^+{}_2$ and $CO^{2+}{}_2$. *Physical Review A*, *50*(5), 3886-3894. doi: 10.1103/PhysRevA.50.3886

Matta, M., Mendillo, M., Withers, P., & Morgan, D. (2015, January). Interpreting

Mars ionospheric anomalies over crustal magnetic field regions using a 2-D ionospheric model. *Journal of Geophysical Research (Space Physics)*, *120*(1), 766-777. doi: 10.1002/2014JA020721

Matta, M., Withers, P., & Mendillo, M. (2013, May). The composition of Mars' topside ionosphere: Effects of hydrogen. *Journal of Geophysical Research (Space Physics)*, *118*(5), 2681-2693. doi: 10.1002/jgra.50104

Mendillo, M., Lollo, A., Withers, P., Matta, M., Pätzold, M., & Tellmann, S. (2011, November). Modeling Mars' ionosphere with constraints from same-day observations by Mars Global Surveyor and Mars Express. *Journal of Geophysical Research (Space Physics)*, *116*(A11), A11303. doi: 10.1029/2011JA016865

Mendillo, M., Narvaez, C., Vogt, M. F., Mayyasi, M., Forbes, J., Galand, M., ... Andersson, L. (2017, September). Sources of Ionospheric Variability at Mars. *Journal of Geophysical Research (Space Physics)*, *122*(9), 9670-9684. doi: 10.1002/2017JA024366

Mohanamanasa, P., Venkateswara Rao, N., Yaswanth, C., & Rao, S. V. B. (2018, July). Magnetically Controlled Density Structures in the Martian Ionosphere: Are they Stably Recurring? *Journal of Geophysical Research (Space Physics)*, *123*(7), 5790-5806. doi: 10.1029/2017JA024920

Morgan, D. D., Gurnett, D. A., Kirchner, D. L., Fox, J. L., Nielsen, E., & Plaut, J. J. (2008, September). Variation of the Martian ionospheric electron density from Mars Express radar soundings. *Journal of Geophysical Research (Space Physics)*, *113*(A9), A09303. doi: 10.1029/2008JA013313

Mukundan, V., Thampi, S. V., Bhardwaj, A., & Krishnaprasad, C. (2020, February). The dayside ionosphere of Mars: Comparing a one-dimensional photochemical model with MAVEN Deep Dip campaign observations. *Icarus*, *337*, 113502. doi: 10.1016/j.icarus.2019.113502

Ness, N. F., Acuña, M. H., Connerney, J. E. P., Kliore, A. J., Breus, T. K., Krymskii, A. M., ... Bauer, S. J. (2000, July). Effects of magnetic anomalies discovered at Mars on the structure of the Martian ionosphere and solar wind interaction as follows from radio occultation experiments. *Journal of Geophysical Research*, *105*(A7), 15991-16004. doi: 10.1029/1999JA000212

Pätzold, M., Tellmann, S., Häusler, B., Hinson, D., Schaa, R., & Tyler, G. L. (2005, November). A Sporadic Third Layer in the Ionosphere of Mars. *Science*, *310*(5749), 837-839. doi: 10.1126/science.1117755

Shinagawa, H., & Cravens, T. E. (1989, June). A one-dimensional multispecies magnetohydrodynamic model of the dayside ionosphere of Mars. *Journal of Geophysical Research*, *94*(A6), 6506-6516. doi: 10.1029/JA094iA06p06506

Siddle, A. G., Mueller-Wodarg, I. C. F., Stone, S. W., & Yelle, R. V. (2019, November). Global characteristics of gravity waves in the upper atmosphere of Mars as measured by MAVEN/NGIMS. *Icarus*, *333*, 12-21. doi: 10.1016/j.icarus.2019.05.021

Thiemann, E. M. B., Chamberlin, P. C., Eparvier, F. G., Templeman, B., Woods, T. N., Bougher, S. W., & Jakosky, B. M. (2017, March). The MAVEN EUVM model of solar spectral irradiance variability at Mars: Algorithms and results. *Journal of Geophysical Research (Space Physics)*, *122*(3), 2748-2767. doi: 10.1002/2016JA023512

Tyler, G. L., Balmino, G., Hinson, D. P., Sjogren, W. L., Smith, D. E., Simpson, R. A., ... Twicken, J. D. (2001, October). Radio science observations with Mars Global Surveyor: Orbit insertion through one Mars year in mapping orbit. *Journal of Geophysical Research*, *106*(E10), 23327-23348. doi: 10.1029/2000JE001348

Venkateswara Rao, N., Mohanamanasa, P., & Rao, S. V. B. (2017, May). Magnetically controlled density structures in the topside layer of the Martian ionosphere. *Journal of Geophysical Research (Space Physics)*, *122*(5), 5619-5629. doi: 10.1002/2016JA023545

Vogt, M. F., Withers, P., Fallows, K., Andersson, L., Girazian, Z., Mahaffy, P. R., ... Jakosky, B. M. (2017, January). MAVEN observations of dayside peak electron densities in the ionosphere of Mars. *Journal of Geophysical Research (Space Physics)*, *122*(1), 891-906. doi: 10.1002/2016JA023473

Wang, J. S., & Nielsen, E. (2003, April). Behavior of the Martian dayside electron density peak during global dust storms. *Planetary and Space Science*, *51*(4-5), 329-338. doi: 10.1016/S0032-0633(03)00015-1

Withers, P. (2009, August). A review of observed variability in the dayside ionosphere of Mars. *Advances in Space Research*, *44*(3), 277-307. doi: 10.1016/j.asr.2009.04.027

Withers, P., Flynn, C. L., Vogt, M. F., Mayyasi, M., Mahaffy, P., Benna, M., ... England, S. (2019, April). Mars's Dayside Upper Ionospheric Composition Is Affected by Magnetic Field Conditions. *Journal of Geophysical Research (Space Physics)*, *124*(4), 3100-3109. doi: 10.1029/2018JA026266

Wu, X. S., Cui, J., Xu, S. S., Lillis, R. J., Yelle, R. V., Edberg, N. J. T., ... Mitchell, D. L. (2019, March). The Morphology of the Topside Martian Ionosphere: Implications on Bulk Ion Flow. *Journal of Geophysical Research (Planets)*, *124*(3), 734-751. doi: 10.1029/2018JE005895

Xu, S., Mitchell, D., Liemohn, M., Fang, X., Ma, Y., Luhmann, J., ... Jakosky, B. (2017, February). Martian low-altitude magnetic topology deduced from MAVEN/SWEA observations. *Journal of Geophysical Research (Space Physics)*, *122*(2), 1831-1852. doi: 10.1002/2016JA023467

Yao, M., Cui, J., Wu, X., Huang, Y., & Wang, W. (2019, January). Variability of the Martian ionosphere from the MAVEN Radio Occultation Science Experiment. *Earth and Planetary Physics*, *3*(4), 283-289. doi: 10.26464/epp2019029

Figure 1.

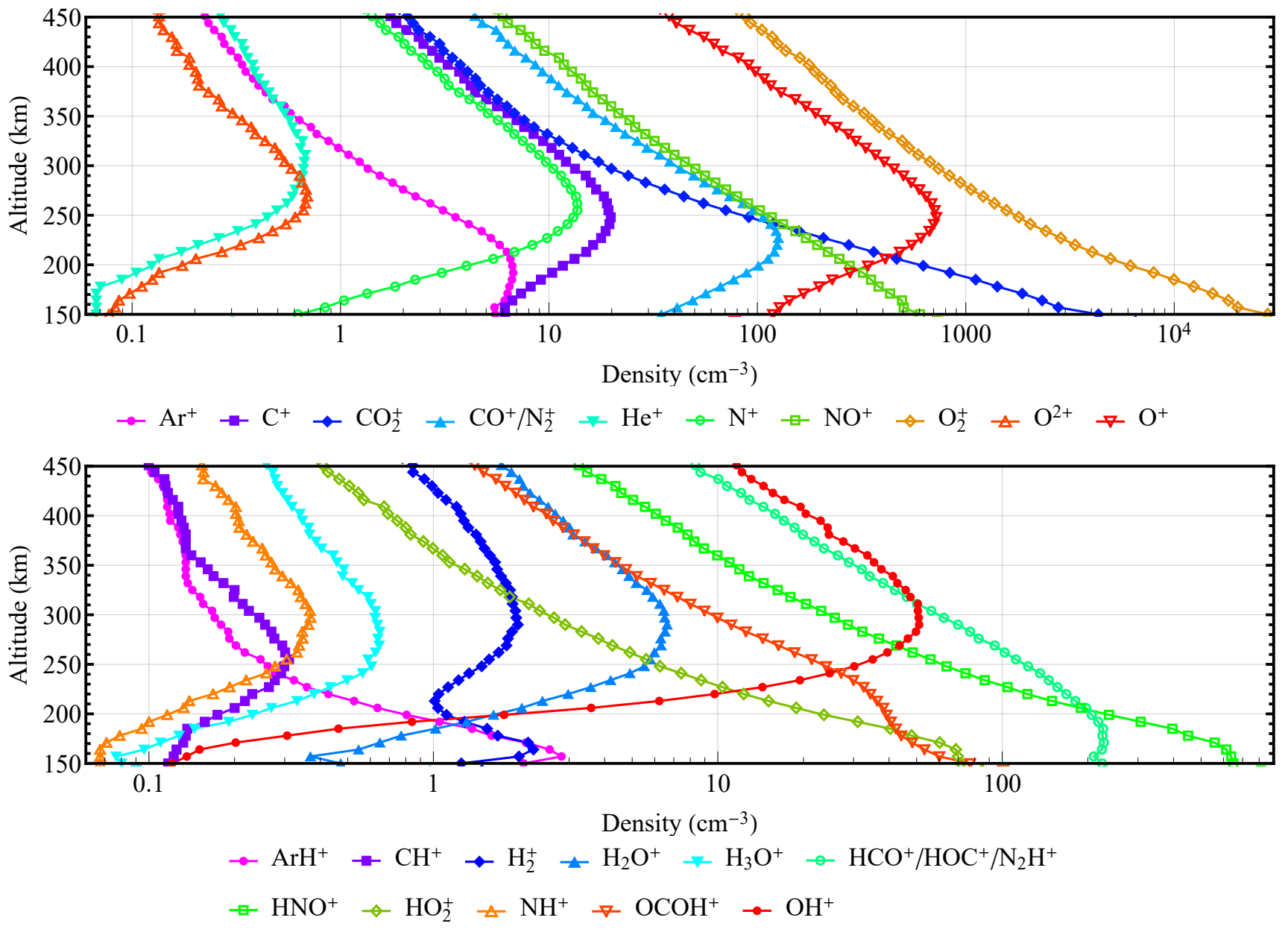
Altitude (km)
450
400
350
300
250
200
150
0.1
1
10
100
1000
10^4
Density (cm^{-3})
Ar^+
C^+
CO_2^+
CO^+/N_2^+
He^+
N^+
NO^+
O_2^+
O^{2+}
O^+
Altitude (km)
450
400
350
300
250
200
150
0.1
1
10
100
Density (cm^{-3})
ArH^+
CH^+
H_2^+
H_2O^+
H_3O^+
$HCO^+/HOC^+/N_2H^+$
HNO^+
HO_2^+
NH^+
$OCOH^+$
OH^+

Figure 2.

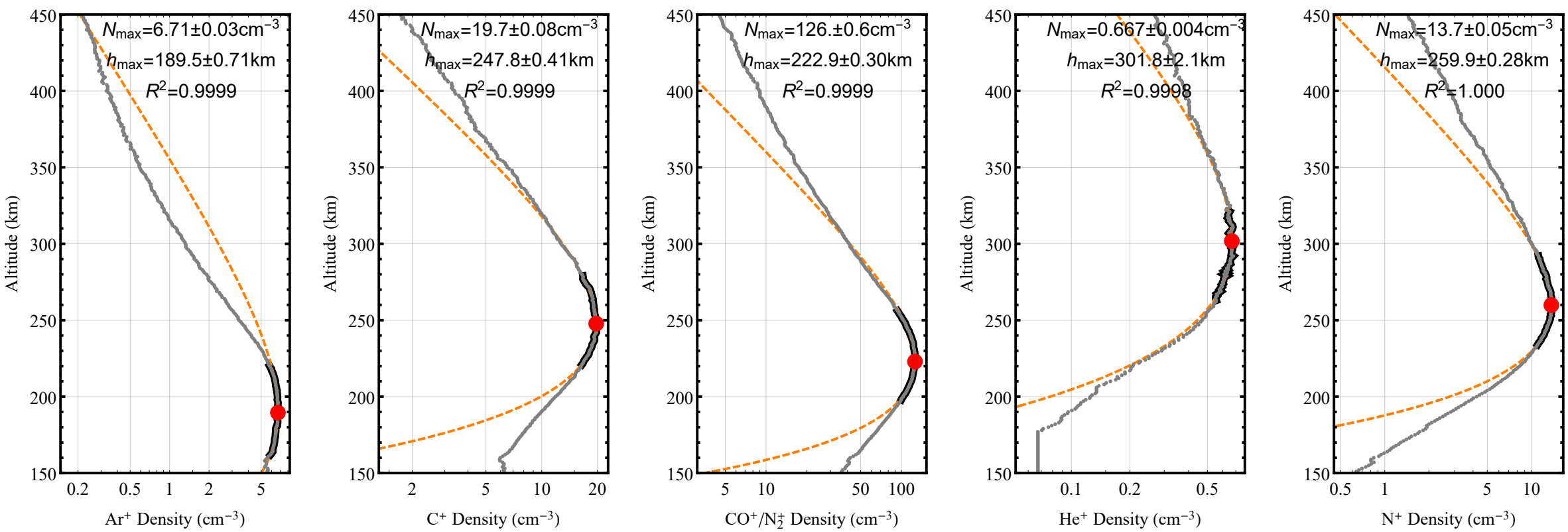
N_{max}=6.71±0.03cm^{-3}
h_{max}=189.5±0.71km
R^2=0.9999
Ar$^+$ Density (cm^{-3})
N_{max}=19.7±0.08cm^{-3}
h_{max}=247.8±0.41km
R^2=0.9999
C$^+$ Density (cm^{-3})
N_{max}=126.±0.6cm^{-3}
h_{max}=222.9±0.30km
R^2=0.9999
CO$^+$/N$_2^+$ Density (cm^{-3})
N_{max}=0.667±0.004cm^{-3}
h_{max}=301.8±2.1km
R^2=0.9998
He$^+$ Density (cm^{-3})
N_{max}=13.7±0.05cm^{-3}
h_{max}=259.9±0.28km
R^2=1.000
N$^+$ Density (cm^{-3})
N_{max}=0.692±0.004cm^{-3}
h_{max}=268.5±0.44km
R^2=0.9999
O^{2+} Density (cm^{-3})
N_{max}=719.±2.cm^{-3}
h_{max}=248.3±0.21km
R^2=1.000
O$^+$ Density (cm^{-3})
N_{max}=2.61±0.09cm^{-3}
h_{max}=158.2±2.2km
R^2=0.9958
ArH$^+$ Density (cm^{-3})
N_{max}=0.303±0.003cm^{-3}
h_{max}=254.1±1.1km
R^2=0.9997
CH$^+$ Density (cm^{-3})
N_{max1}=2.12±0.09cm^{-3}
h_{max1}=166.8±1.3km
R^2=0.9939
N_{max2}=1.95±0.008cm^{-3}
h_{max2}=299.5±1.7km
R^2=0.9999
H$_2^+$ Density (cm^3)
N_{max}=6.51±0.04cm^{-3}
h_{max}=287.5±1.3km
R^2=0.9999
H$_2$O$^+$ Density (cm^{-3})
N_{max}=0.641±0.007cm^{-3}
h_{max}=292.0±2.6km
R^2=0.9995
H$_3$O$^+$ Density (cm^{-3})
N_{max}=227.±2.cm^{-3}
h_{max}=174.7±1.2km
R^2=0.9997
HCO$^+$/HOC$^+$/N$_2$H$^+$ Density (cm^{-3})
N_{max}=0.364±0.003cm^{-3}
h_{max}=295.0±1.5km
R^2=0.9998
NH$^+$ Density (cm^{-3})
N_{max}=51.1±0.2cm^{-3}
h_{max}=297.6±0.73km
R^2=0.9999
OH$^+$ Density (cm^{-3})
Altitude (km)

Figure 3.

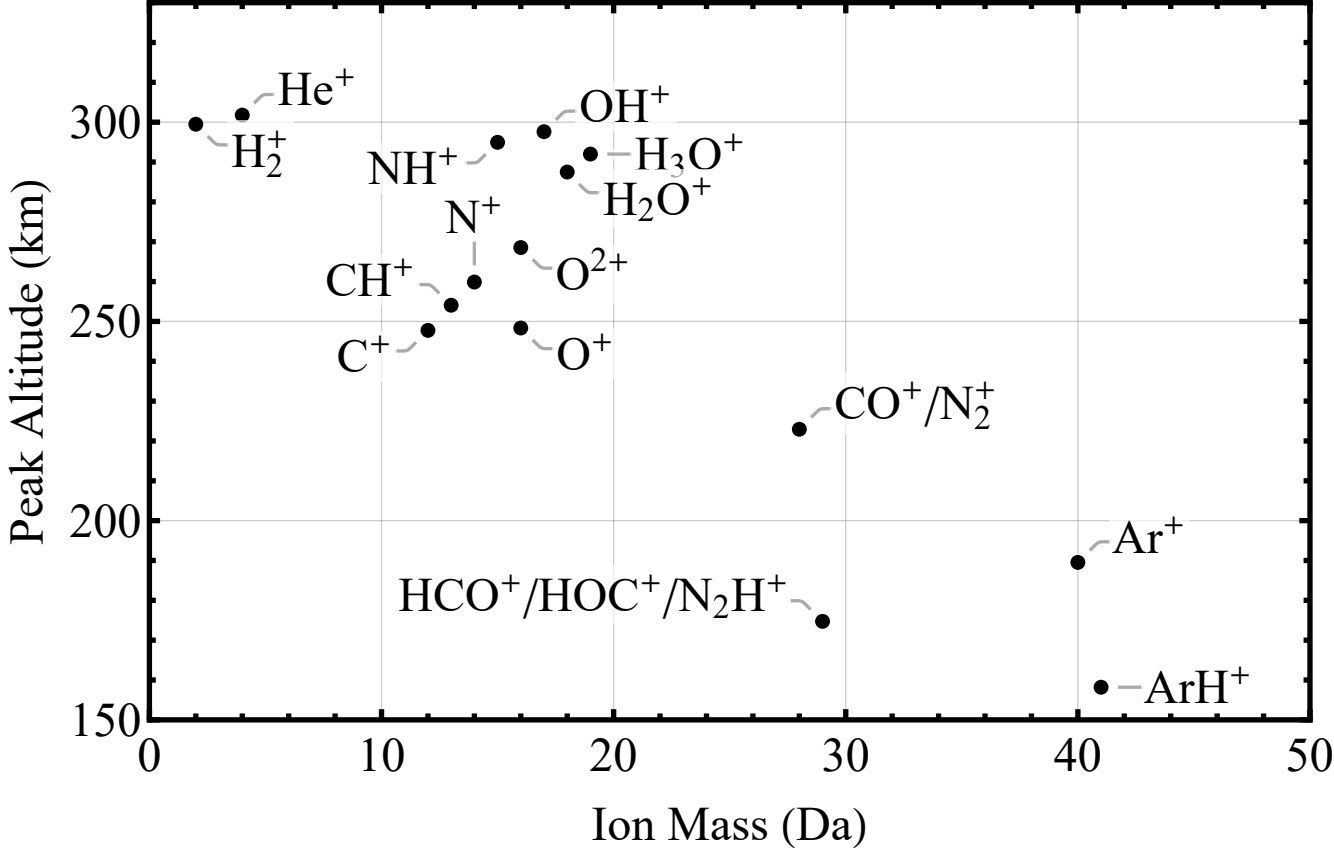
Peak Altitude (km)
300
250
200
150
0
10
20
30
40
50
Ion Mass (Da)
He^+
H_2^+
OH^+
NH^+
H_3O^+
H_2O^+
N^+
CH^+
O^{2+}
C^+
O^+
CO^+/N_2^+
Ar^+
$HCO^+/HOC^+/N_2H^+$
ArH^+

Figure 4.

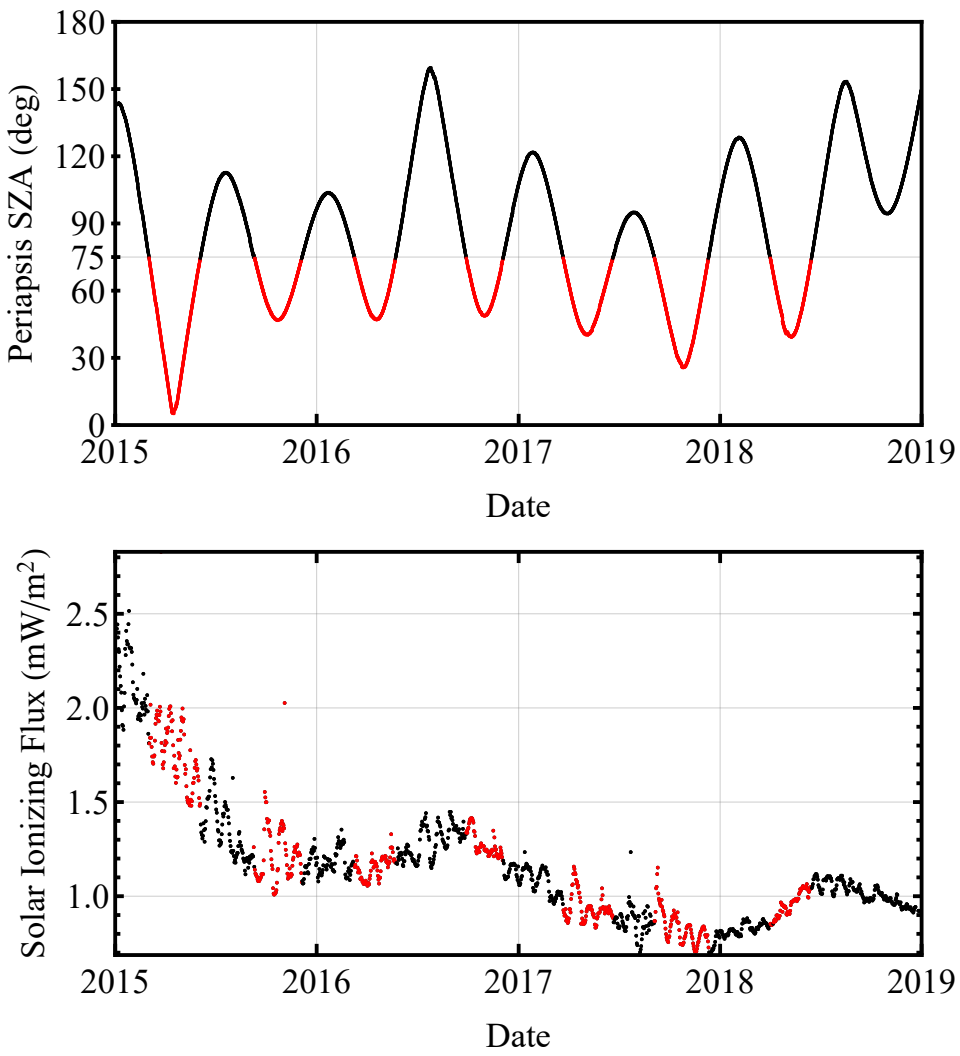
Periapsis SZA (deg)
180
150
120
90
75
60
30
0
2015
2016
2017
2018
2019
Date
Solar Ionizing Flux (mW/m^2)
2.5
2.0
1.5
1.0
2015
2016
2017
2018
2019
Date

Figure 5.

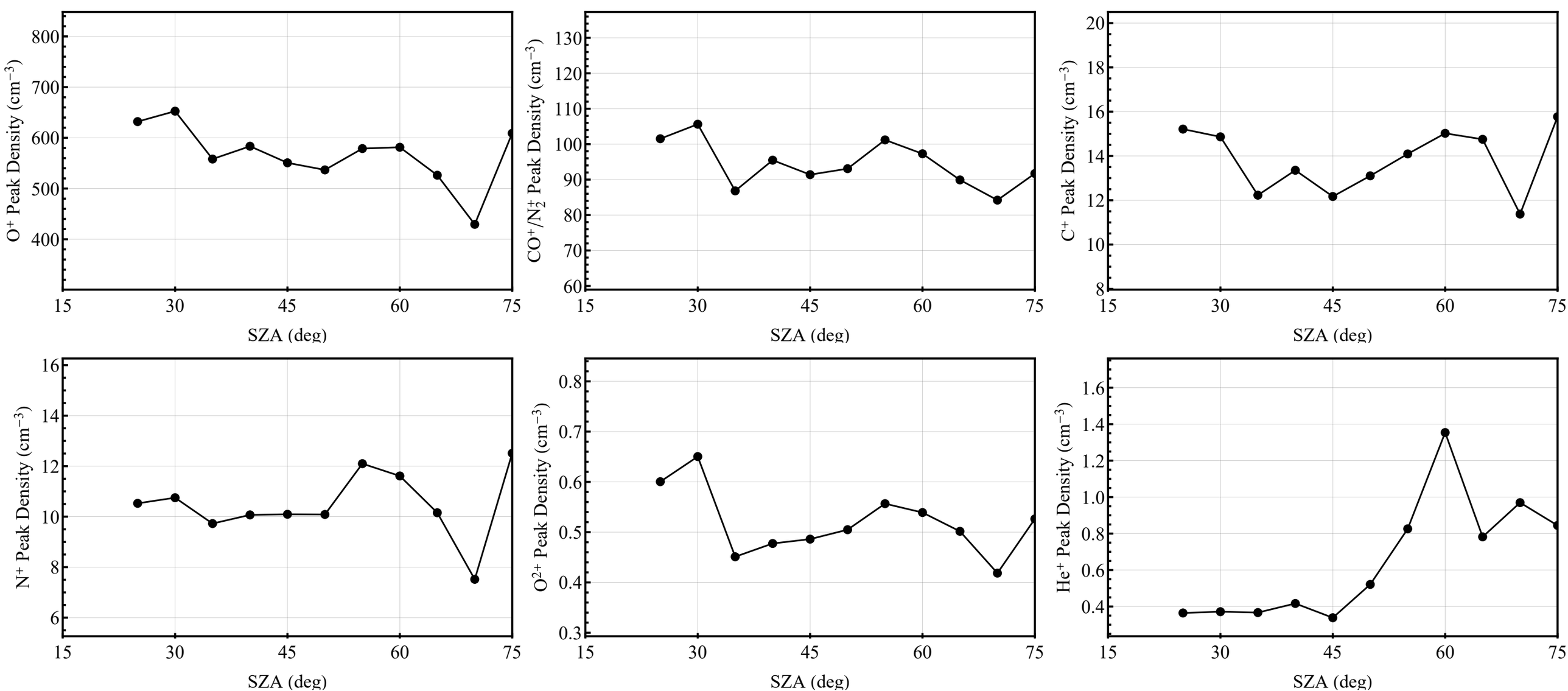
O+ Peak Density (cm−3)
CO+/N2+ Peak Density (cm−3)
C+ Peak Density (cm−3)
N+ Peak Density (cm−3)
O2+ Peak Density (cm−3)
He+ Peak Density (cm−3)
SZA (deg)

Figure 6.

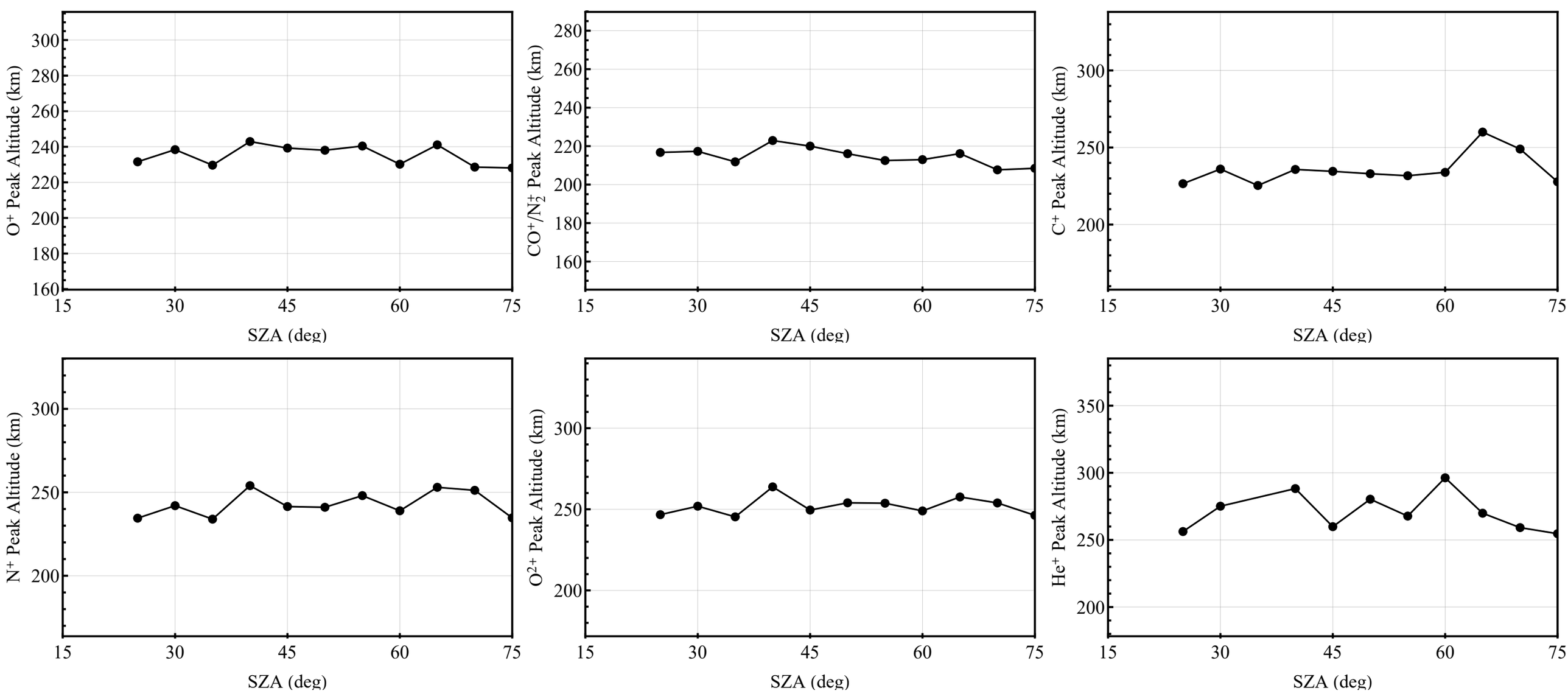
O+ Peak Altitude (km)
CO+/N2+ Peak Altitude (km)
C+ Peak Altitude (km)
N+ Peak Altitude (km)
O2+ Peak Altitude (km)
He+ Peak Altitude (km)
SZA (deg)

Figure 7.

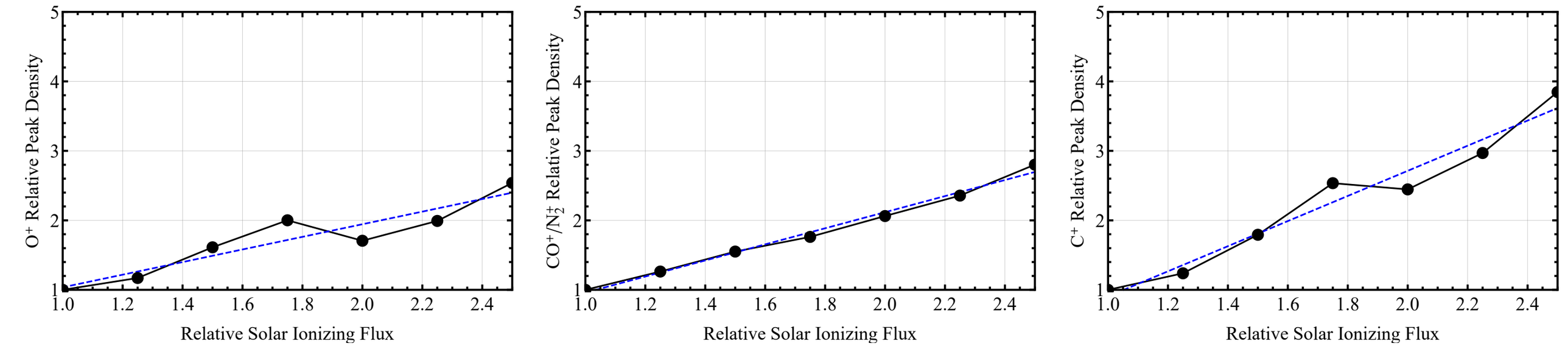
O+ Relative Peak Density
CO+/N2+ Relative Peak Density
C+ Relative Peak Density
N+ Relative Peak Density
O2+ Relative Peak Density
He+ Relative Peak Density
Relative Solar Ionizing Flux
1.0
1.2
1.4
1.6
1.8
2.0
2.2
2.4
1
2
3
4
5

Figure 8.

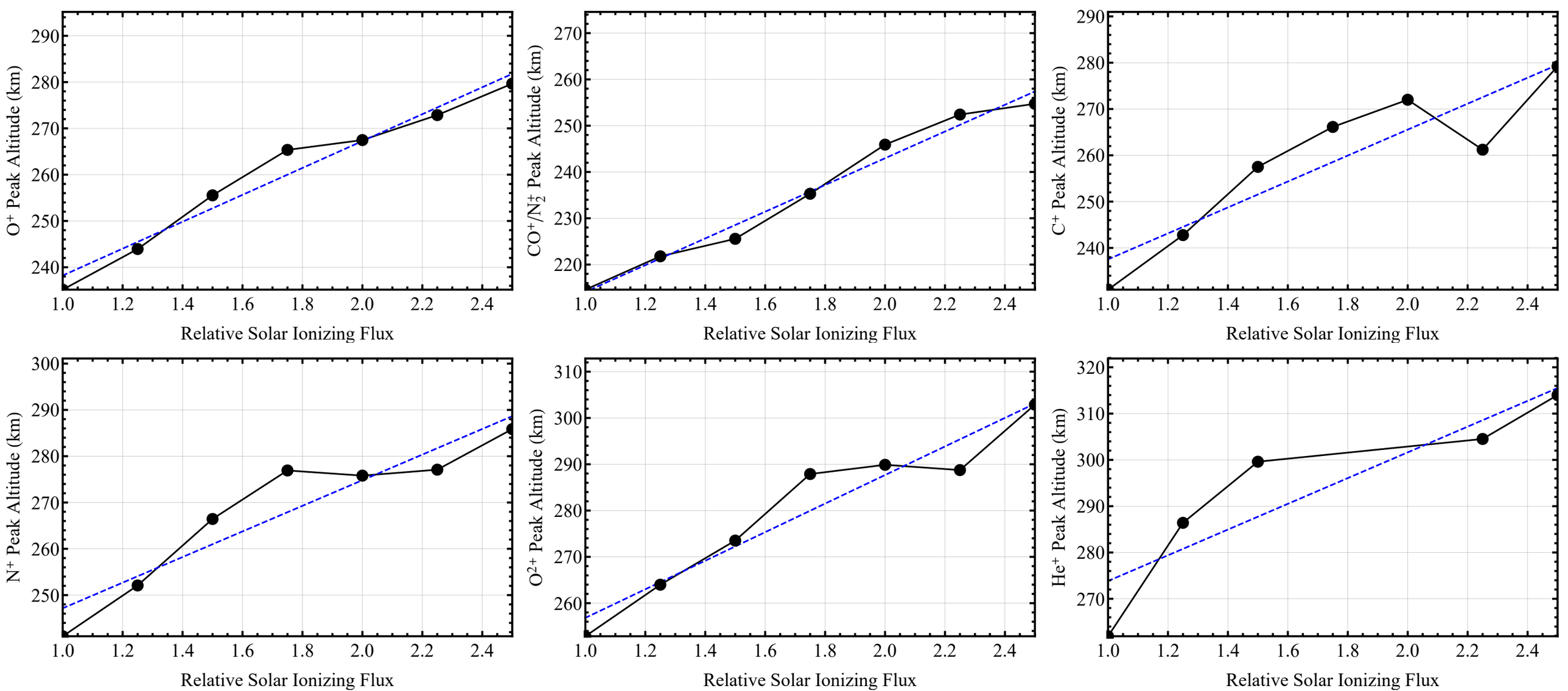
O+ Peak Altitude (km)
290
280
270
260
250
240
1.0
1.2
1.4
1.6
1.8
2.0
2.2
2.4
Relative Solar Ionizing Flux
CO+/N2+ Peak Altitude (km)
270
260
250
240
230
220
Relative Solar Ionizing Flux
C+ Peak Altitude (km)
290
280
270
260
250
240
Relative Solar Ionizing Flux
N+ Peak Altitude (km)
300
290
280
270
260
250
Relative Solar Ionizing Flux
O2+ Peak Altitude (km)
310
300
290
280
270
260
Relative Solar Ionizing Flux
He+ Peak Altitude (km)
320
310
300
290
280
270
Relative Solar Ionizing Flux

Figure 9.

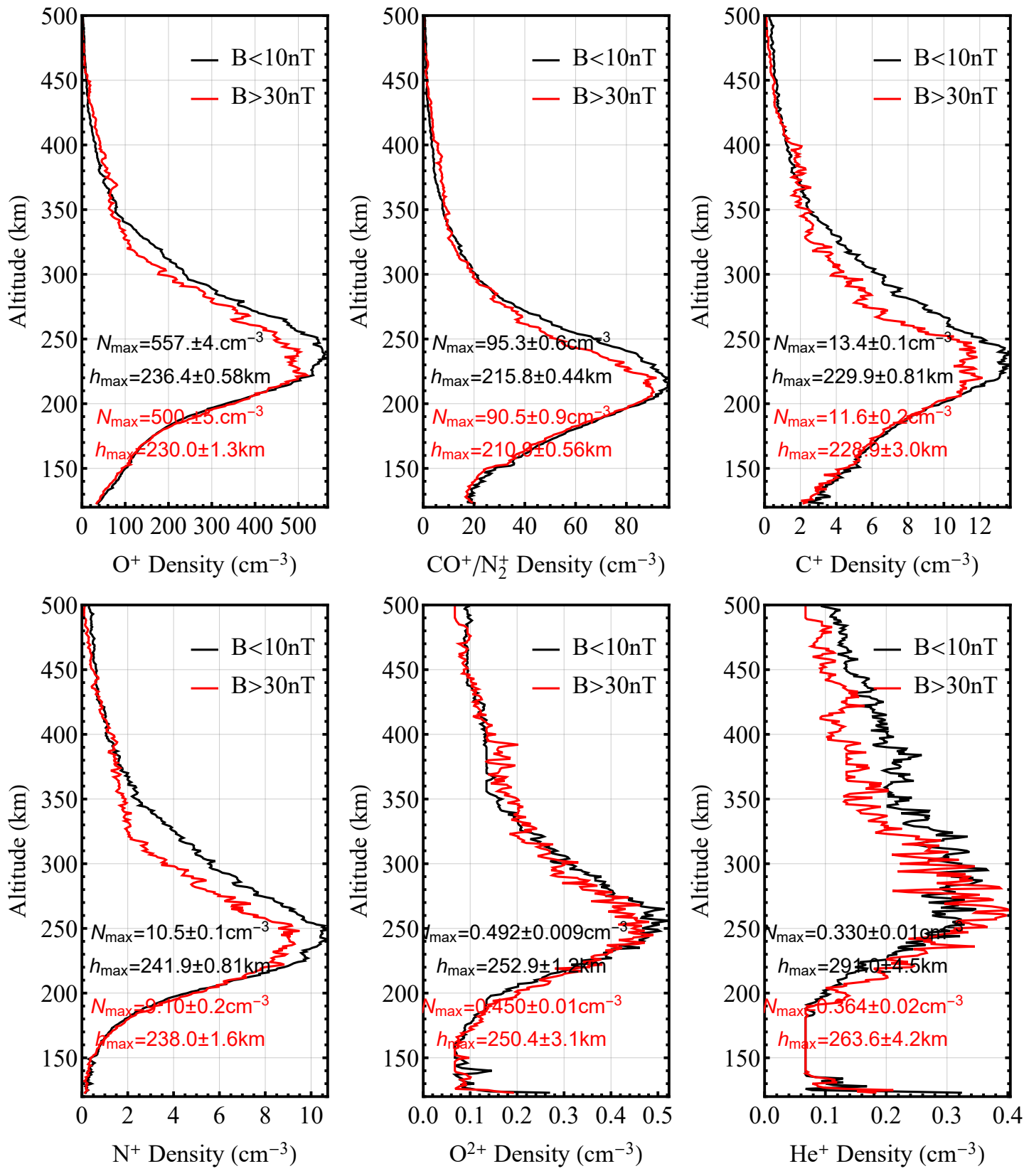
B<10nT
B>30nT
Altitude (km)
O+ Density (cm−3)
Nmax=557.±4.cm−3
hmax=236.4±0.58km
Nmax=500.±5.cm−3
hmax=230.0±1.3km
CO+/N2+ Density (cm−3)
Nmax=95.3±0.6cm−3
hmax=215.8±0.44km
Nmax=90.5±0.9cm−3
hmax=210.9±0.56km
C+ Density (cm−3)
Nmax=13.4±0.1cm−3
hmax=229.9±0.81km
Nmax=11.6±0.2cm−3
hmax=228.9±3.0km
N+ Density (cm−3)
Nmax=10.5±0.1cm−3
hmax=241.9±0.81km
Nmax=9.10±0.2cm−3
hmax=238.0±1.6km
O2+ Density (cm−3)
Nmax=0.492±0.009cm−3
hmax=252.9±1.2km
Nmax=0.450±0.01cm−3
hmax=250.4±3.1km
He+ Density (cm−3)
Nmax=0.330±0.01cm−3
hmax=291.0±4.5km
Nmax=0.364±0.02cm−3
hmax=263.6±4.2km